

Deep Gradient Learning for Efficient Camouflaged Object Detection

Ge-Peng Ji¹, Deng-Ping Fan^{✉2}, Yu-Cheng Chou¹, Dengxin Dai², Alexander Liniger² and Luc Van Gool²

¹School of Computer Science, Wuhan University, Wuhan, China.

²Computer Vision Lab, ETH Zürich, Zürich, Switzerland.

Abstract

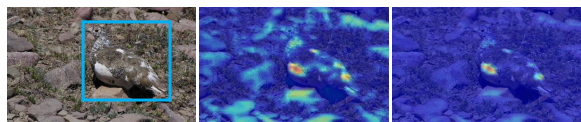
This paper introduces **DGNet**, a novel deep framework that exploits object gradient supervision for camouflaged object detection (COD). It decouples the task into two connected branches, *i.e.*, a context and a texture encoder. The essential connection is the gradient-induced transition, representing a soft grouping between context and texture features. Benefiting from the simple but efficient framework, DGNet outperforms existing state-of-the-art COD models by a large margin. Notably, our efficient version, **DGNet-S**, runs in real-time (80 fps) and achieves comparable results to the cutting-edge model JCSOD-CVPR₂₁ with only 6.82% parameters. Application results also show that the proposed DGNet performs well in polyp segmentation, defect detection, and transparent object segmentation tasks. Codes will be made available at <https://github.com/GewelsJI/DGNet>.

Keywords: Camouflaged object detection, object gradient, soft grouping, image segmentation.

1 Introduction

Camouflaged object detection [1, 2] (COD) aims to segment objects with either artificial or natural patterns where objects ‘perfectly’ blend into the background to avoid being discovered [2]. Several successful applications, such as polyp segmentation [3–5], lung infection segmentation [6–8], and recreational art [9, 10], have shown COD’s scientific and practical value.

Recent studies [11–14] present compelling results based on the supervision of the *whole object-level* ground-truth mask. Later, various sophisticated techniques, *e.g.*, boundary-based [15–17] and uncertainty-guided [18, 19],



Camouflaged Image (a) Object Boundary (b) Object Gradient

Fig. 1 Feature visualization of learned texture. We observe that the proposed DGNet-S under the object boundary supervision (a) contains diffused noises in the background. By contrast, object gradient supervision (b) enforces the network focus on the regions where the intensity changes dramatically.

were developed to augment COD’s underlying representations. However, features learned from boundary-supervised or uncertainty-based models usually respond to the sparse edge of camouflage objects, thereby introducing noisy features, especially for complex scenes (see Fig. 1-a). Besides, the boundaries of camouflaged objects are always

[✉] Corresponding author. The major part of this work was done while Ge-Peng Ji was an intern at the Inception Institute of Artificial Intelligence (IIAI) mentored by Deng-Ping Fan.

‘indefinable’ or ‘fuzzy’; thus, they do not be pop-out from a quick visual scanning. We notice that despite the object’s camouflage, there are still some clues left, shown in the first column of Fig. 1 (white speckles). Instead of extracting only boundary or uncertainty regions, we are interested in how the network mines these ‘discriminative patterns’ inside the object.

From this perspective, we present our *deep gradient network* (**DGNet**) via the explicit supervision of the *object-level* gradient map. The underlying hypothesis is that there are some intensity changes inside the camouflaged objects. To ease the learning task, we decouple the DGNet into two connected branches, *i.e.*, a context and a texture encoder. The former can be viewed as a contextual semantics learner, while the latter acts as a structural texture extractor. In this way, we can alleviate the feature ambiguity between the high-level and low-level features extracted from the individual branch. To sufficiently aggregate the above two discriminative features generated by the two branches, we further design a gradient-induced transition (GIT) module that collaboratively ensembles the multi-source feature space at different group scales (*i.e.*, soft grouping). Fig. 1-b shows that our DGNet can detect texture patterns while suppressing the background noise by an intensity-sensitive strategy focusing on the intra-region of a camouflaged object.

Extensive experiments on three challenging COD benchmarks illustrate that the proposed DGNet achieves state-of-the-art (SOTA) performance without introducing any complicated structures. Furthermore, we implement an efficient version DGNet-S with 8.3M parameters, which achieves the fastest inference speed (80 fps) among COD-related baselines. Notably, it only has 6.82% parameters compared to the cutting-edge model JCSOD-CVPR₂₁ [19] while achieving comparable performance. These results show that DGNet significantly narrows the gap between scientific research and practical application. Three downstream applications (see Sec. 5) of our DGNet also support this conclusion. The major **contributions** of this paper are summarized as:

- We introduce a novel deep gradient-based framework, dubbed **DGNet**, for addressing the camouflaged object detection task.

- We propose a **gradient-induced transition** to automatically group features from the context and texture branches according to the soft grouping strategy.
- We present **three applications** and achieve good performance, including polyp segmentation, defect detection, and transparent object segmentation.

2 Prior Works

Traditional methods detect camouflaged objects via extracting various hand-crafted features between the camouflaged areas and their backgrounds, which calculate the 3D convexity [20], co-occurrence matrix [21], expectation-maximization statistics [22], optical flow [23], and Gaussian mixture model [24]. Those methods work well for simple backgrounds, while the performance degrades drastically for complex backgrounds.

CNN-based approaches could be generally categorized into three strategies: *a) Attention-based strategy*: Sun *et al.* [25, 26] introduce a network with an attention-induced cross-level fusion module to integrate multi-scale features and a dual-branch global context module to mine multi-scale contextual information. To mimic the detection process of predators, Mei *et al.* [11] develop PFNet, which contains a positioning and focusing module to conduct the identification. [16, 27] propose delicate structures such as covariance matrices of feature and multivariate calibration components to improve the robustness of the network. Kajiura *et al.* [28] improve the detection accuracy via exploring the uncertainties of pseudo-edge and pseudo-map labels. Zhuge *et al.* [29] propose a cube-alike architecture for COD, which accompanies by attention fusion and X-shaped connection to sufficiently integrate multiple-layer features. *b) Two-stage strategy*: Search and identification strategy [1] is an early practice to model the COD task. In [2], the neighbour connection decoder and group-reversal attention are introduced in SINet [1] to boost the performance further. *c) Joint-learning strategy*: ANet [30] is an early attempt to utilize the classification and segmentation scheme for COD. LSR [12] and JCSOD [19] have recently renewed the joint-learning framework by introducing camouflaged ranking or learning from salient objects to camouflaged objects. ZoomNet [31] is a mixed-scale

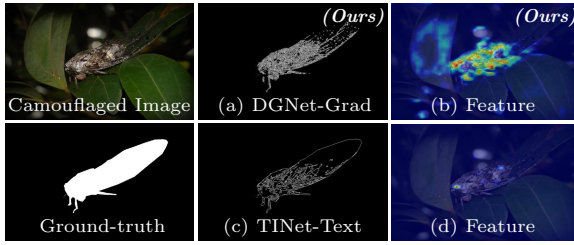


Fig. 2 In comparison with the texture label proposed in TINet [34], our object gradient label (a) keeps more geometric cues inside the camouflaged object. DGNet under the supervision of texture label (c) fails to infer attentive regions (d) since the imbalanced distribution of sparse pixels (*e.g.*, thin object boundaries). Notably, such improvement exerts our DGNet more robust with the reliable auxiliaries (*e.g.*, feature in (b)).

triplet network, which employs the zoom strategy to learn the discriminative camouflaged semantics. **Transformer-based & Graph-based** models are two recent technology trends. Recently, Mao *et al.* [32] introduce the concept of difficulty-aware learning based on the Transformer for both camouflaged and salient object detection. UGTR [18] explicitly utilizes the probabilistic representational model to learn the uncertainties of the camouflaged object under the Transformer framework. In addition, Cheng *et al.* [33] are the first to collect a video dataset for COD and utilise the Transformer-based framework to exploit both short-term dynamics and long-term temporal consistency to detect dynamic camouflaged objects. Later, Zhai *et al.* [15] design the mutual graph learning model, which decouples one input into different features for roughly locating the target and accurately capturing its boundary.

Remarks. By contrast, our work excavates the texture information via learning the object-level gradient rather than using boundary-aware or uncertainty-aware modelling. The biologically inspired idea behind this is that the abundant gradient cues inside the camouflaged object deserve to be explored, while the sparse boundary cues are insufficient to achieve this. As shown in Fig. 2, we also note that the recent work [34] tries to utilize the texture cues while they discard excessive object gradient cues due to different threshold settings of the Canny detector. In short, this paper aims at designing an elegant framework towards efficient COD with more concise ideas (*i.e.*, object gradient learning). More experimental validations are discussed in Sec. 4.3.

3 Deep Gradient Network

As discussed in [35], the low-level and high-level features occupy an equal role in the scene understanding. As suggested by [36], it is not encouraged to encode them simultaneously. As shown in Fig. 3, we propose to model the camouflaged representations with two separate encoders, a context and a texture encoder.

3.1 Context Encoder

For a camouflaged input image $\mathcal{I} \in \mathbb{R}^{3 \times H \times W}$, we use the widely used EfficientNet [37] as the context encoder to obtain the pyramid features $\{\mathbf{X}_i\}_{i=1}^5$.

Dimensional Reduction. Inspired by [3], we adopt the following two steps to ensure efficient element-wise operations between different levels in the decoding stage: *a)* we only pick out the top-three features (*i.e.*, when $i = 3, 4, 5$), which retain the affluent semantics of the visual scene. *b)* we further utilize two stacked ConvBR¹ layers with $C_i \times 3 \times 3$ filters to reduce the dimension of each candidate feature to C_i , contributing to easing the computational burden of subsequent operations. The final outputs are three context features $\{\mathbf{X}_i^R\}_{i=3}^5 \in \mathbb{R}^{C_i \times H_i \times W_i}$, where C_i , $H_i = \frac{H}{2^i}$, and $W_i = \frac{W}{2^i}$ denote the channel, height, and width of the feature maps.

3.2 Texture Encoder

We also introduce a tailored texture branch supervised by the object-level gradient map, which compensates for the pattern degradation caused by the top-three context features' weak representation of geometric textures.

Object Gradient Generation. An image gradient describes the directional change in an image's intensity or color between adjacent positions, which is widely applied for edge detection [40] and super-resolution [41]. The right part of Fig. 3 presents four widely used types of supervision labels. The object boundary (c) and image gradient (e) can be directly generated by calculating the gradient of the object-level ground-truth \mathbf{Z}^C (b) and raw image (a), respectively. However, the raw image gradient map (e), which contains irrelevant background noises may mislead the optimization

¹In this paper, ConvBR denotes the standard convolutional layer followed with a BN [38] layer and a ReLU [39] layer.

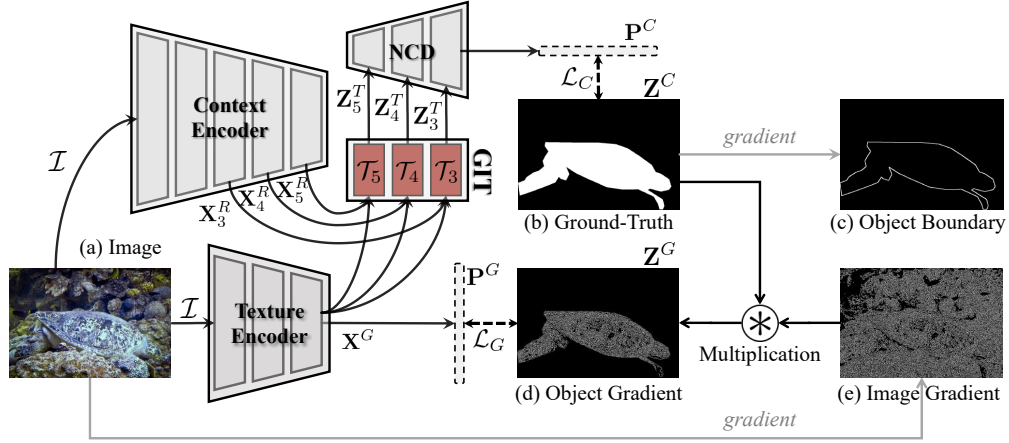


Fig. 3 Overall pipeline of the proposed DGNet. It consists of two connected learning branches, *i.e.*, context encoder (Sec. 3.1) and texture encoder (Sec. 3.2). Then, we introduce a gradient-induced transition (GIT) (Sec. 3.3) to collaboratively aggregate the feature that is derived from the above two encoders. Finally, a neighbor connected decoder (NCD) [2] is adopted to generate the prediction P^C (Sec. 3.4).

Table 1 Details of the tailored texture encoder. k : kernel size, c : output channels, s : stride, and p : zero-padding. Here, we set the channel $C_g = 32$ as default setting.

Layer	Input Size	Output Size	Component	k	c	s	p
#01	$3 \times H \times W$	$64 \times \frac{H}{2} \times \frac{W}{2}$	ConvBR	7	64	2	3
#02	$64 \times \frac{H}{2} \times \frac{W}{2}$	$64 \times \frac{H}{4} \times \frac{W}{4}$	ConvBR	3	64	2	1
#03	$64 \times \frac{H}{4} \times \frac{W}{4}$	$C_g \times \frac{H}{8} \times \frac{W}{8}$	ConvBR	3	C_g	2	1
#04	$C_g \times \frac{H}{8} \times \frac{W}{8}$	$1 \times \frac{H}{8} \times \frac{W}{8}$	ConvBR	1	1	1	0

process when serving as the supervision signal for texture learning. To address this problem, we introduce a novel camouflage learning paradigm which uses the object-level gradient map Z^G (d) as supervision, which holds both the gradient cues of the object’s boundaries and interior regions. This process could be formulated as:

$$Z^G = \mathcal{F}_E(\mathcal{I}(x, y)) \otimes Z^C, \quad (1)$$

where \mathcal{F}_E represents the standard Canny edge detector [42] for an input \mathcal{I} with discrete pixel coordinates (x, y) . \otimes means the element-wise multiplication.

Texture Encoder. Because low-level features with a high resolution will introduce a computational burden, we design a tailored lightweight encoder instead of utilizing an out-of-box backbone. We obtain the texture feature $X^G \in \mathbb{R}^{C_g \times H_g \times W_g}$ from layer#03 (see Table 1). However, we supervise the following layer#04 with the object-level gradient Z^G . We keep the texture feature with larger resolution (*i.e.*, $H_g = \frac{H}{8}$

and $W_g = \frac{W}{8}$) since the features with smaller resolution would discard most geometric details.

3.3 Gradient-Induced Transition

The latent correlation between context and texture features offers great potential for adaptive fusion, rather than adopting naive fusion strategies (*e.g.*, concatenation and addition operations). Here, we design a flexible plug-and-play *gradient-induced transition (GIT)* module (see Fig. 4), which views the texture feature as the auxiliaries in the multi-source aggregation from a group-wise perspective. Specifically, it comprises the following three steps.

Gradient-Induced Group Learning. Inspired by [2], we first adopt the gradient-induced group learning strategy, which splits three context features $\{X_i^R\}_{i=3}^5$ and a texture feature X^G into fixed groups along the channel dimension. For each X_i^R and X^G pair, this strategy can be formulated as:

$$\begin{aligned} \{X_{i,m}^R\}_{m=1}^M &\in \mathbb{R}^{K_i \times H_i \times W_i} \leftarrow X_i^R \in \mathbb{R}^{C_i \times H_i \times W_i}, \\ \{X_m^G\}_{m=1}^M &\in \mathbb{R}^{K_g \times H_g \times W_g} \leftarrow X^G \in \mathbb{R}^{C_g \times H_g \times W_g}, \end{aligned} \quad (2)$$

where \leftarrow is the feature grouping operation. $K_i = C_i/M$ and $K_g = C_g/M$ denote the channel number of each feature group, and M is the corresponding number of groups. Then, we periodically arrange groups of context features $X_{i,m}^R$ and texture features X_m^G , which generates the regrouped

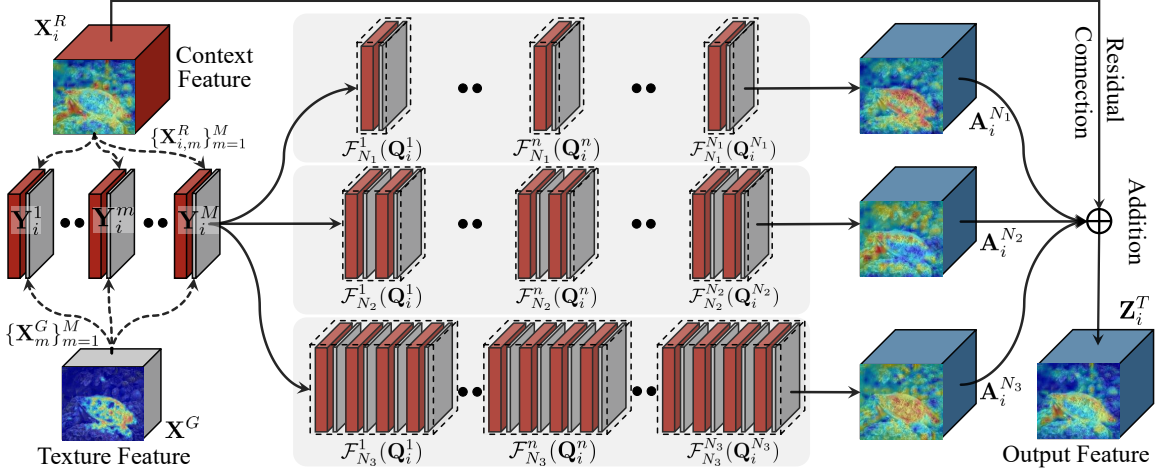


Fig. 4 Illustration of the proposed gradient-induced transition (GIT).

feature \mathbf{Q}_i via:

$$\mathbf{Q}_i \in \mathbb{R}^{(C_i+C_g) \times H_i \times W_i} = \langle \mathbf{Y}_i^1; \dots; \mathbf{Y}_i^m; \dots; \mathbf{Y}_i^M \rangle, \quad (3)$$

where $\langle \cdot; \cdot \rangle$ means the channel-wise feature concatenation. Here, the m -th sub-component \mathbf{Y}_i^m is derived from:

$$\mathbf{Y}_i^m \in \mathbb{R}^{(K_i+K_g) \times H_i \times W_i} = \langle \mathcal{F}_\downarrow(\mathbf{X}_m^G); \mathbf{X}_{i,m}^R \rangle, \quad (4)$$

where the down-sampling operation $\mathcal{F}_\downarrow(\cdot)$ ensures the spatial resolution of \mathbf{X}_m^G matches $\mathbf{X}_{i,m}^R$.

Soft Grouping Strategy. The naive feature fusion strategies may ignore the correlation or distinctiveness between context and texture representations due to lacking further multi-source interactions. Inspired by the parallel design introduced in [43] for capturing objects at multiple scales, we propose using a soft grouping strategy to provide parallel nonlinear projections at multiple fine-grained sub-spaces, which enables the network to probe multi-source representations jointly. It is defined as:

$$\mathbf{A}_i^N = \langle \mathcal{F}_N^1(\mathbf{Q}_i^1); \dots; \mathcal{F}_N^n(\mathbf{Q}_i^n) \dots \mathcal{F}_N^N(\mathbf{Q}_i^N) \rangle, \quad (5)$$

where $\mathcal{F}_N^n(\mathbf{Q}_i^n) \in \mathbb{R}^{(C_i/N) \times H_i \times W_i} = f_n(\mathbf{Q}_i^n, \omega_n)$ intentionally introduce soft non-linearity at each multi-source sub-space. The projection function f_n is implemented by a convolutional layer with C_i filters of shape of $\frac{(C_i+C_g)}{N} \times 1 \times 1$, which is parameterized by learnable weights ω_n . Here, \mathbf{Q}_i^n is the n -th subset of the regrouped feature \mathbf{Q}_i that is divided into N groups.

Parallel Residual Learning. We further introduce residual learning [44] in a parallel manner at different group-aware scales. Consequently, we can define the GIT function $\mathcal{T}_i(\cdot, \cdot)$ (see the red block in Fig. 3) as:

$$\mathbf{Z}_i^T = \mathcal{T}_i(\mathbf{X}_i^R, \mathbf{X}_i^G) = \mathbf{X}_i^R \oplus \sum_N \mathbf{A}_i^N, \quad (6)$$

where $N \in \{N_1, N_2, N_3\}$ denotes a set of scaling factors for different groups, which will be discussed in Sec. 4.3. \oplus means the element-wise addition, and \sum denotes a sum of multiple terms. The final output is $\{\mathbf{Z}_i^T\}_{i=3}^5 \in \mathbb{R}^{C_i \times H_i \times W_i}$.

3.4 Learning Details

Decoder. Given the context features $\{\mathbf{X}_i^R\}_{i=3}^5$, we firstly apply the GIT function $\mathcal{T}_i(\cdot, \cdot)$ (see Equ.(6)) to get the output features $\{\mathbf{Z}_i^T\}_{i=3}^5$. To exploit the above gradient-induced features in \mathbf{Z}_i^T more efficiently, we utilize the neighbour connection decoder (NCD) [2] to generate the final prediction, which enables feature propagation from high to low levels. Thus, the final prediction \mathbf{P}^C can be derived from $\mathbf{P}^C \in \mathbb{R}^{1 \times H \times W} = \text{NCD}(\mathbf{Z}_3^T, \mathbf{Z}_4^T, \mathbf{Z}_5^T)$.

Loss Function. The overall optimization objective is defined as:

$$\mathcal{L} = \mathcal{L}_C(\mathbf{P}^C, \mathbf{Z}^C) + \mathcal{L}_G(\mathbf{P}^G, \mathbf{Z}^G), \quad (7)$$

where \mathcal{L}_C and \mathcal{L}_G represent the loss of final prediction \mathbf{P}^C and gradient prediction \mathbf{P}^G , respectively. For the former, it is formulated as $\mathcal{L}_C =$

Table 2 Hyper-parameter settings of the proposed DGNet-S and DGNet.

Model	Backbone	C_i	C_g	M	$\{N_1, N_2, N_3\}$
DGNet-S	EfficientNet-B1	32	32	8	$\{8, 16, 32\}$
DGNet	EfficientNet-B4	64	32	8	$\{4, 8, 16\}$

$\mathcal{L}_{IoU}^w + \mathcal{L}_{BCE}^w$, where \mathcal{L}_{IoU}^w and \mathcal{L}_{BCE}^w represent the weighted intersection-over-union (IoU) loss and the weighted binary cross-entropy (BCE) loss, respectively. They assign the adaptive weight for each pixel according to its difficulty to focus on the global structure and pay more attention to the hard pixels. The definitions of these losses are the same as in [1, 2, 45] and their effectiveness has been proven in the field of binary segmentation. For the latter, we employ the standard mean squared error loss function.

Training Settings. The proposed DGNet is implemented in the PyTorch [46]/Jittor [47] toolbox and trained/inferred on a single NVIDIA RTX TITAN GPU. The model parameters are initialized with the strategy of [48], and we initialize the backbone with the model weights pre-trained on ImageNet [49] to prevent over-fitting. We discard the last stage of Conv1×1, pooling, and fully connected layers in the EfficientNet [37] backbone and extract the features from the top-three lateral outputs, including **stage-4** (\mathbf{X}_3), **stage-6** (\mathbf{X}_4), and **stage-8** (\mathbf{X}_5). Considering the performance-efficiency trade-off, we instantiate two variants to adapt the specific requirement under various computational overheads (refer to Table 2).

We train our model in an end-to-end manner, using Adam [50]. The cosine annealing part of the SGDR strategy [51] is used to adjust the learning rate, where the minimum/maximum learning rate and the maximum adjusted iteration are set to $10^{-5}/10^{-4}$ and 20, respectively. The batch size is set to 12, and the maximum training epoch is 100. During training, we resize each image to 352×352 and feed it into DGNet with four data augmentation techniques: color enhancement, random flipping, random cropping, and random rotation.

Testing Settings. Once the network is well-trained, we resize the input images to 352×352 and test our DGNet-S and DGNet on three unseen test datasets. We take the final output \mathbf{P}^C as the prediction map without any heuristic post-processing techniques, such as DenseCRF [52].

4 Experiments

4.1 Benchmarking

Datasets. There are three popular datasets in the COD field: *a)* CAMO [30] has 1,250 camouflaged images and is divided into CAMO-Train (1,000 samples) and CAMO-Test (250 samples). *b)* COD10K [2] is the largest COD dataset till now, consisting of COD10K-Train (3,040 images) and COD10K-Test (2,026 images). It is downloaded from multiple free photography websites, covering 5 super-classes and 69 sub-classes. *c)* NC4K-Test [12], as the largest testing dataset, includes 4,121 samples, which are used to evaluate the models' generalization ability. Following the protocol of [2], we train our model on the hybrid dataset (*i.e.*, COD10K-Train + CAMO-Train) with 4,040 samples and evaluate our method on above three benchmarks (see Table 3).

Metrics. Following [2], we use five commonly used metrics for the evaluation: structure measure (\mathcal{S}_α) [53], enhanced-alignment measure (E_ϕ^{mx}) [54, 55], F-measure (F_β^{mx}) [56, 57], weighted F-measure (F_β^w) [58], and mean absolute error (\mathcal{M}). Besides, the precision-recall (PR) curve [59] are obtained by varying different thresholds from [0, 255]. Similar to this thresholding strategy, F-measure and E-measure curves are also reported. Moreover, we adopt three criteria to measure the model's complexity and efficiency: the number of model parameters, measured in Millions (M), the number of multiply-accumulate (MACs) operations, measured in Giga (G), and inference speed measured in frames per second (fps).

Competitors. We compare our model with 20 SOTA competitors (see Table 3), including 8 SOD-based and 12 COD-based. For a fair comparison, all results were either taken from the public website or produced by retraining the models on the same training dataset with default settings.

4.2 Results and Analysis

Quantitative Results. As shown in Table 3, DGNet achieves the promising performance in terms of all metrics. Especially, the gradient-based learning strategy helps to improve the completeness of predictions, providing a 2.6% gain of F_β^w on CAMO-Test than rank@1 model SINetV2 [2].

Quantitative Curves. As shown in Fig. 5, we plot the precision-recall (1st row), F-measure (2nd

Table 3 Quantitative results in terms of full metrics for cutting-edge competitors, including 8 SOD-related and 12 COD-related, on three COD-related test datasets. @ \mathcal{R} is the ranking of the current metric, and Mean @ \mathcal{R} indicates the mean ranking of all metrics. Note that $E_{\phi}^{mx}/F_{\beta}^{mx}$, $E_{\phi}^{mn}/F_{\beta}^{mn}$, and $E_{\phi}^{ad}/F_{\beta}^{ad}$ denote the maximum, mean, and adaptive value of E-measure/F-measure, respectively. \uparrow/\downarrow denotes that the higher/lower the score, the better. All the benchmark results are available at [OneDrive](#) (3.54 GB).

	Metric	SOD-related Models								COD-related Models												DGNNet-S	
		EGNet	SCRN	CPD	CSNet-R	F3Net	UCNet	ITSD	MINet	SINet	PraNet	BAS	C2FNet	TINet	UGTR	PFNet	S-MGL	R-MGL	LSR	JCSOD	SINetV2	Ours	DGNNet
NC4K-Test [12]	$S_{\alpha} \uparrow$.777	.830	.788	.750	.780	.811	.811	.805	.808	.822	.817	.838	.829	.839	.829	.829	.833	.840	.842	.847	.845	.857
	@ \mathcal{R}	21	9	19	22	20	16	15	18	17	13	14	7	12	6	11	10	8	5	4	2	3	1
	$E_{\phi}^{mx} \uparrow$.864	.897	.865	.793	.848	.886	.883	.881	.883	.888	.872	.904	.890	.899	.898	.893	.893	.907	.907	.914	.913	.922
	@ \mathcal{R}	20	9	19	22	21	14	15	17	16	13	18	6	12	7	8	11	10	5	4	2	3	1
	$E_{\phi}^{mn} \uparrow$.841	.854	.804	.773	.824	.871	.845	.846	.871	.876	.859	.897	.879	.874	.888	.863	.867	.895	.898	.903	.902	.911
	@ \mathcal{R}	19	16	21	22	20	11	18	17	12	9	15	5	8	10	7	14	13	6	4	2	3	1
	$E_{\phi}^{ad} \uparrow$.826	.864	.842	.812	.853	.883	.855	.876	.882	.871	.868	.898	.880	.886	.892	.884	.889	.902	.903	.898	.899	.907
	@ \mathcal{R}	21	17	20	22	19	11	18	14	12	15	16	6	13	9	7	10	8	3	2	5	4	1
	$F_{\beta}^{mx} \uparrow$.639	.698	.632	.603	.656	.729	.680	.705	.723	.724	.732	.762	.734	.747	.745	.731	.740	.766	.771	.770	.764	.784
	@ \mathcal{R}	20	17	21	22	19	13	18	16	15	14	11	6	10	7	8	12	9	4	2	3	5	1
	$F_{\beta}^{mn} \uparrow$.731	.793	.738	.669	.719	.782	.762	.768	.775	.786	.782	.810	.793	.807	.799	.797	.800	.815	.816	.823	.819	.833
	@ \mathcal{R}	20	11	19	22	21	15	18	17	16	13	14	6	12	7	9	10	8	5	4	2	3	1
	$F_{\beta}^{mn} \uparrow$.696	.757	.695	.655	.705	.775	.729	.753	.769	.762	.772	.795	.773	.787	.784	.777	.782	.804	.806	.805	.799	.814
	@ \mathcal{R}	20	16	21	22	19	11	18	17	14	15	13	6	12	7	8	10	9	4	2	3	5	1
$F_{\beta}^{ad} \uparrow$.671	.744	.709	.672	.710	.776	.717	.763	.768	.753	.767	.788	.766	.779	.779	.771	.778	.802	.803	.792	.789	.803	
@ \mathcal{R}	22	17	20	21	19	10	18	15	12	16	13	6	14	8	7	11	9	3	2	4	5	1	
$\mathcal{M} \downarrow$.075	.059	.074	.088	.070	.055	.064	.060	.058	.059	.058	.049	.055	.052	.053	.055	.052	.048	.047	.048	.047	.042	
@ \mathcal{R}	21	15	20	22	19	10	18	17	14	16	13	6	12	8	9	11	7	5	2	4	3	1	
Mean@ \mathcal{R}	21	15	20	22	19	12	18	17	16	13	14	6	11	7	8	10	9	5	2	3	4	1	
CAMO-Test [30]	$S_{\alpha} \uparrow$.732	.779	.726	.771	.711	.739	.750	.737	.745	.769	.749	.796	.781	.785	.782	.772	.775	.787	.800	.820	.826	.839
	@ \mathcal{R}	20	10	21	13	22	18	15	19	17	14	16	5	9	7	8	12	11	6	4	3	2	1
	$E_{\phi}^{mx} \uparrow$.820	.850	.801	.849	.780	.820	.830	.818	.829	.837	.808	.864	.848	.854	.855	.842	.842	.854	.873	.895	.907	.915
	@ \mathcal{R}	17	9	21	10	22	18	15	19	16	14	20	5	11	8	6	13	12	7	4	3	2	1
	$E_{\phi}^{mn} \uparrow$.800	.797	.723	.795	.741	.787	.780	.767	.804	.824	.796	.854	.836	.823	.842	.807	.812	.838	.859	.882	.893	.901
	@ \mathcal{R}	14	15	22	17	21	18	19	20	13	9	16	5	8	10	6	12	11	7	4	3	2	1
	$E_{\phi}^{ad} \uparrow$.811	.848	.810	.847	.802	.811	.830	.826	.825	.833	.806	.864	.845	.859	.852	.850	.847	.855	.865	.875	.892	.901
	@ \mathcal{R}	18	10	20	12	22	19	15	16	17	14	21	5	13	6	8	9	11	7	4	3	2	1
	$F_{\beta}^{mx} \uparrow$.604	.643	.553	.642	.564	.640	.610	.613	.644	.663	.646	.719	.678	.686	.695	.664	.673	.696	.728	.743	.754	.769
	@ \mathcal{R}	20	15	22	16	21	17	19	18	14	12	13	5	9	8	7	11	10	6	4	3	2	1
	$F_{\beta}^{mn} \uparrow$.688	.738	.667	.740	.630	.708	.694	.683	.708	.728	.703	.771	.745	.754	.758	.739	.740	.753	.779	.801	.810	.822
	@ \mathcal{R}	19	13	21	10	22	15	18	20	16	14	17	5	9	7	6	12	11	8	4	3	2	1
	$F_{\beta}^{mn} \uparrow$.670	.705	.614	.705	.616	.700	.663	.667	.702	.710	.692	.762	.728	.738	.746	.721	.726	.744	.772	.782	.792	.806
	@ \mathcal{R}	18	13	22	14	21	16	20	19	15	12	17	5	9	8	6	11	10	7	4	3	2	1
$F_{\beta}^{ad} \uparrow$.667	.733	.678	.730	.661	.716	.692	.704	.712	.715	.696	.764	.729	.749	.751	.733	.738	.756	.779	.779	.786	.804	
@ \mathcal{R}	21	10	20	12	22	14	19	17	16	15	18	5	13	8	7	11	9	6	4	3	2	1	
$\mathcal{M} \downarrow$.109	.090	.114	.092	.109	.094	.102	.096	.092	.094	.096	.080	.087	.086	.085	.089	.088	.080	.073	.070	.063	.057	
@ \mathcal{R}	21	12	22	13	20	15	19	18	14	16	17	6	9	8	7	11	10	5	4	3	2	1	
Mean@ \mathcal{R}	20	12	21	13	22	16	18	19	15	14	17	5	9	8	7	11	10	6	4	3	2	1	
COD10K-Test [2]	$S_{\alpha} \uparrow$.736	.789	.748	.778	.739	.776	.767	.769	.776	.789	.802	.813	.793	.818	.800	.811	.814	.804	.809	.815	.810	.822
	@ \mathcal{R}	22	13	20	15	21	17	19	18	16	14	10	5	12	2	11	6	4	9	8	3	7	1
	$E_{\phi}^{mx} \uparrow$.855	.880	.842	.871	.819	.867	.861	.864	.874	.879	.870	.900	.878	.891	.890	.890	.890	.892	.891	.906	.905	.911
	@ \mathcal{R}	20	11	21	15	22	17	19	18	14	12	16	4	13	7	10	9	8	5	6	2	3	1
	$E_{\phi}^{mn} \uparrow$.810	.817	.766	.810	.795	.857	.808	.823	.864	.861	.855	.890	.861	.853	.877	.845	.852	.880	.884	.887	.888	.896
	@ \mathcal{R}	19	17	22	18	21	11	20	16	8	10	12	2	9	13	7	15	14	6	5	4	3	1
	$E_{\phi}^{ad} \uparrow$.753	.789	.768	.791	.818	.867	.787	.837	.867	.839	.869	.886	.848	.850	.868	.851	.865	.882	.882	.863	.868	.877
	@ \mathcal{R}	22	19	21	18	17	8	20	16	9	15	5	1	14	13	7	12	10	3	2	11	6	4
	$F_{\beta}^{mx} \uparrow$.517	.575	.509	.569	.544	.633	.557	.601	.631	.629	.677	.686	.635	.667	.660	.655	.666	.673	.684	.680	.672	.693
	@ \mathcal{R}	21	17	22	18	20	13	19	16	14	15	5	2	12	8	10	11	9	6	3	4	7	1
	$F_{\beta}^{mn} \uparrow$.633	.699	.634	.679	.609	.691	.658	.672	.691	.704	.729	.743	.712	.742	.725	.733	.738	.732	.738	.752	.743	.759
	@ \mathcal{R}	21	14	20	17	22	16	19	18	15	13	10	3	12	5	11	8	7	9	6	2	4	1
	$F_{\beta}^{mn} \uparrow$.582	.651	.582	.635	.593	.681	.615	.654	.679	.671	.715	.723	.679	.712	.701	.702	.711	.715	.721	.718	.710	.728
	@ \mathcal{R}	22	17	21	18	20	12	19	16	13	15	6	2	14	7	11	10	8	5	3	4	9	1
$F_{\beta}^{ad} \uparrow$.526	.593	.555	.589	.588	.673	.573	.639	.667	.640	.707	.703	.652	.671	.676	.667	.681	.699	.705	.682	.680	.698	
@ \mathcal{R}	22	17	21	18	19	10	20	16	12	15	1	3	14	11	9	13	7	4	2	6	8	5	
$\mathcal{M} \downarrow$.061	.047	.058	.047	.051	.042	.051	.043	.043	.045	.038	.036	.042	.035	.040	.037	.035	.037	.035	.037	.036	.033	
@ \mathcal{R}	22	18	21	17	20	13	19	15	14	16	10	5	12	4	11	9	3	8	2	7	6	1	
Mean@ \mathcal{R}	22	16	21	18	20	14	19	17	13	15	9	2	12	8	10	11	7	6	3	4	5	1	

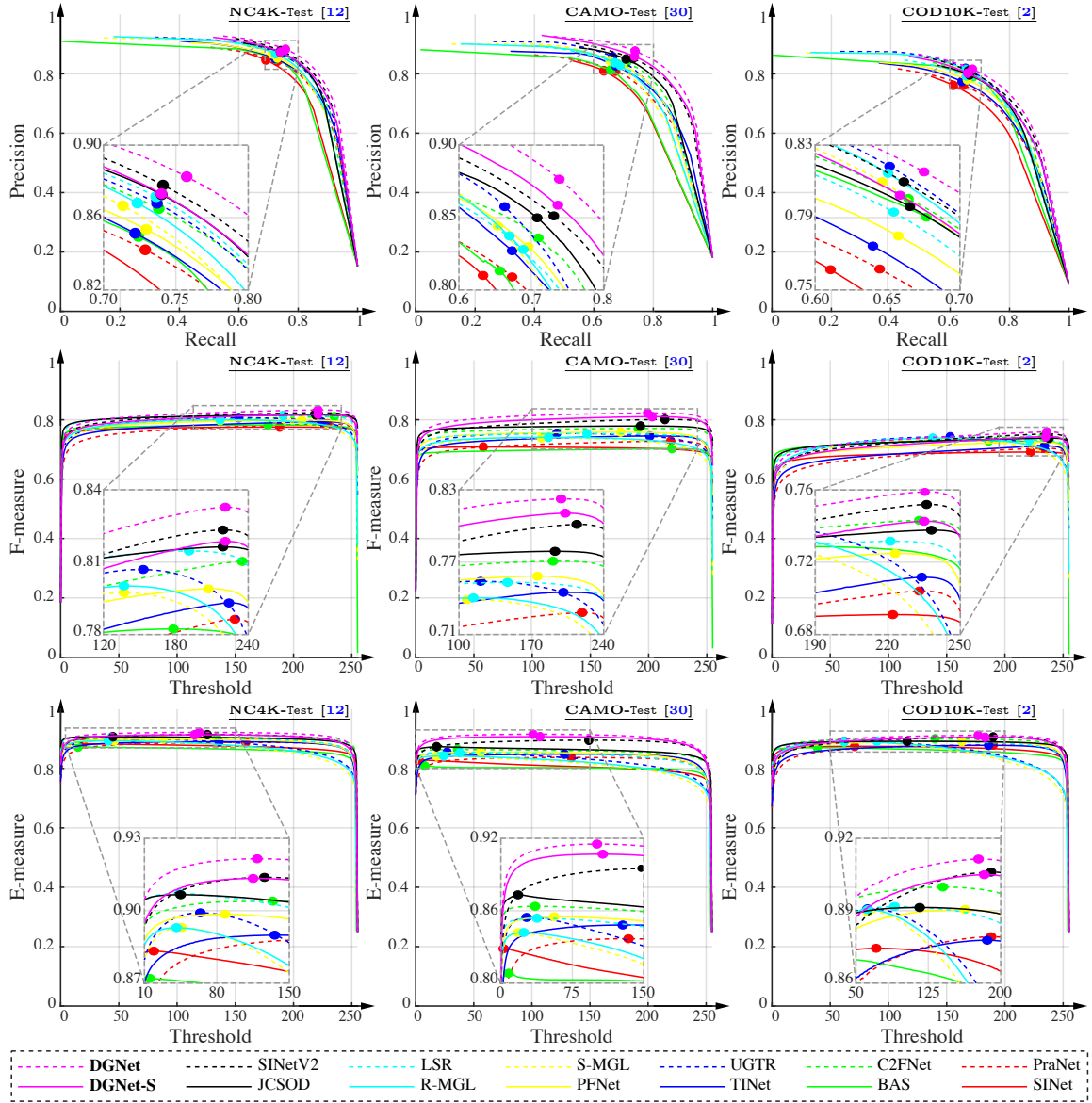


Fig. 5 The PR curves (1st row), F-measure curves (2nd row), and E-measure curves (3rd row) of COD-related competitors on three popular datasets. The closer the PR curve is to the upper-right corner, the better the performance is. The higher the F-measure/E-measure curve is, the better the performance the model works. Best viewed in color.

row), and E-measure (3rd row) curves of all COD-related competitors via varying with different thresholds. All comparisons show that our curves with magenta solid/dotted line are significantly better than other methods on three datasets.

Qualitative Results. The visual comparison of four top-tier COD baselines and our DGNet are shown in Fig. 6. Interestingly, these competitors fail to provide complete segmentation results for the camouflaged objects that touch the image

boundary. By contrast, our approach can precisely locate the target region and provide exact predictions due to the gradient learning strategy. **Efficiency Analysis.** To better unveil the trade-off, two instances consistently obtain the best trade-off compared to existing competitors (see Fig. 7). DGNet outperforms cutting-edge model SINetV2 [2] with a large margin (F_β^w : +2.6%). Notably, our efficient instance DGNet-S performs better than JCSOD [19], with 113.33M fewer

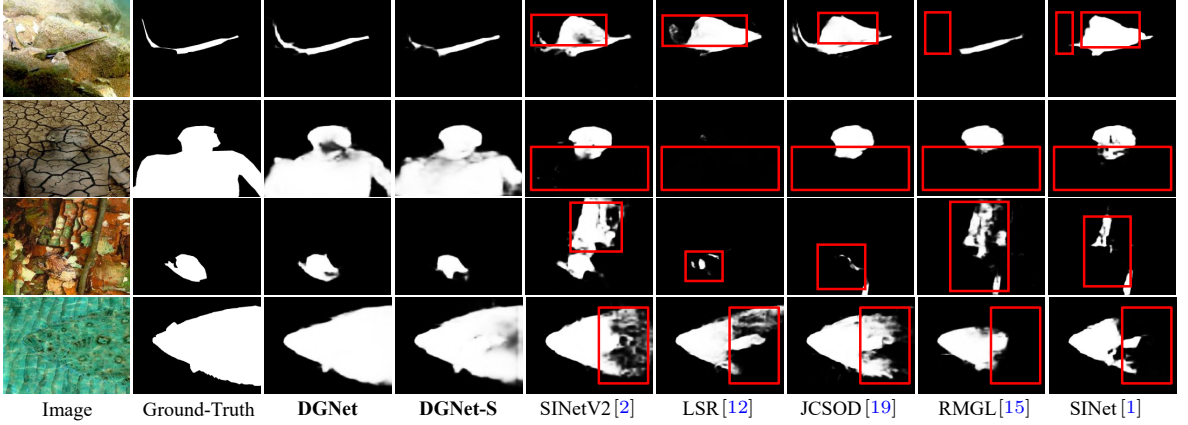


Fig. 6 Visualization of popular COD baselines and the proposed DGNet. More results are presented in our [GitHub](#).

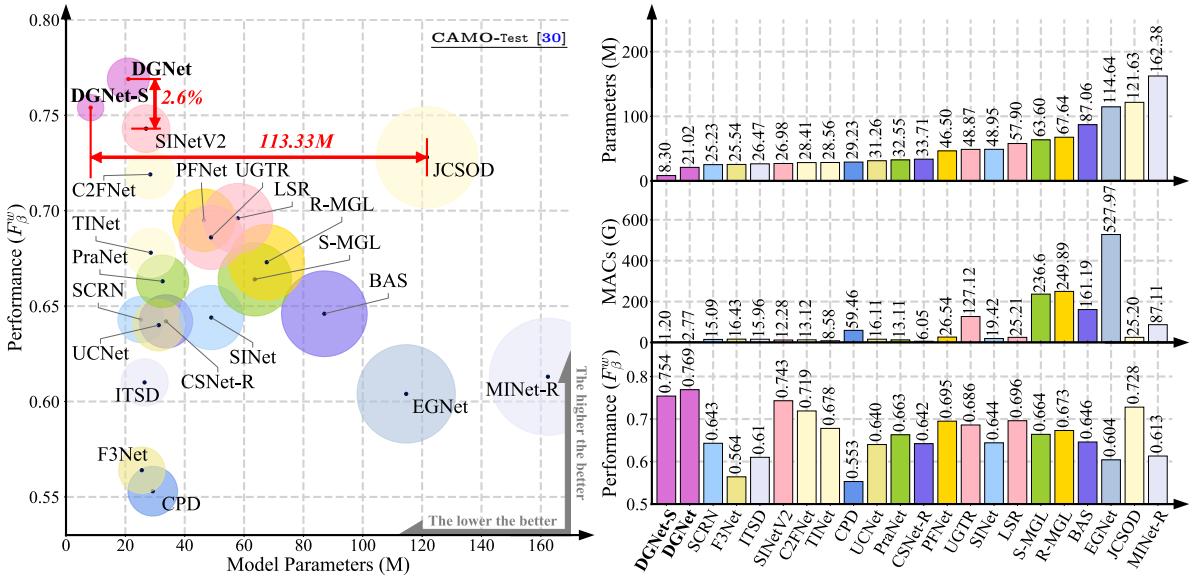


Fig. 7 (Left) We present the scatter relationship between the performance (F_{β}^w) and parameters of all competitors on CAMO-Test [30]. The larger size of the colored scatter point, the heavier the model parameters. (Right) We also report the parallel histogram comparison of model's parameters, MACs, and performance (F_{β}^w). Best viewed in color.

parameters. Besides, we also report the run-time comparison of all COD-related competitors in Table 4, which are tested on an NVIDIA RTX TITAN GPU. It clearly illustrates that DGNet-S and DGNet can achieve super real-time inference speed (*i.e.*, 80 fps & 58 fps).

4.3 Ablation Study

We further ablate the core modules to verify the effectiveness of each part and configuration. For ecological reasons, we select the DGNet-S as the base model in this section.

Contribution of Base Network. In Table 5-(a), we remove the texture encoder and GIT from DGNet-S and term it as the base network (#01). Compared to it, our DGNet-S (#S) significantly improves the performance while slightly increasing the model parameters by 0.06M.

Configuration of Dimensional Reduction. We change the channel C_i to 16 (#02), 32 (#S), 64 (#03), and 128 (#04) and find that more parameters may lead to performance saturation. To achieve the best trade-off between resource and speed, we choose $C_i=32$ as the default setting.

Table 4 Inference speed (fps) among 12 COD-related models and the proposed two instances (*i.e.*, DGNet-S and DGNet).

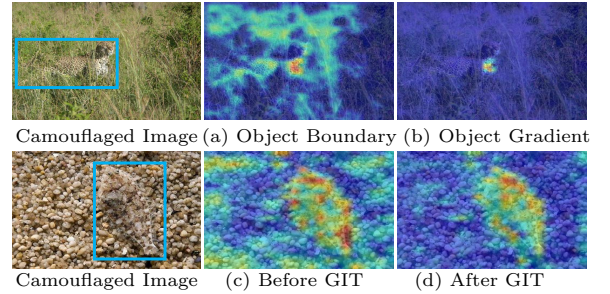
Model	DGNet-S	DGNet	SINetV2 [2]	JCSOD [19]	LSR [12]	R-MGL [15]	S-MGL [15]
Input Size	352×352	352×352	352×352	352×352	352×352	473×473	473×473
Speed (fps)	80	58	68	43	31	9	13
Model	PFNet [11]	UGTR [18]	TINet [34]	C2FNet [25]	BAS [67]	PraNet [3]	SINet [1]
Input Size	416×416	473×473	352×352	352×352	288×288	352×352	352×352
Speed (fps)	78	15	50	68	31	73	63

Table 5 Ablation studies. #Para and #MACs denote the parameters and multiply-accumulate operations of model.

No.	Variant	Efficiency		NC4K-Test [12]			CAMO-Test [30]			COD10K-Test [2]		
		#Para	#MACs	$S_\alpha \uparrow$	$F_\beta^w \uparrow$	$\mathcal{M} \downarrow$	$S_\alpha \uparrow$	$F_\beta^w \uparrow$	$\mathcal{M} \downarrow$	$S_\alpha \uparrow$	$F_\beta^w \uparrow$	$\mathcal{M} \downarrow$
#S	DGNet-S	8.30M	1.20G	.845	.764	.047	.826	.754	.063	.810	.672	.036
(a) Base Network \rightarrow see Sec. 3.1												
#01	Base	8.24M	0.58G	.834	.676	.061	.814	.670	.072	.793	.550	.049
(b) Configuration of Dimensional Reduction \rightarrow see Sec. 3.1												
#02	$C_i = 16$	8.00M	0.81G	.842	.758	.048	.824	.749	.066	.806	.663	.037
#03	$C_i = 64$	9.36M	2.69G	.845	.764	.047	.827	.748	.065	.812	.673	.036
#04	$C_i = 128$	13.30M	8.55G	.847	.768	.046	.828	.751	.062	.810	.672	.036
(c) Network Decoupling Strategy \rightarrow see Sec. 3.2												
#05	w/ \mathbf{X}_2	8.24M	0.59G	.840	.712	.055	.822	.701	.074	.805	.597	.043
(d) Should we use \mathbf{Z}^G as supervision? \rightarrow see Equ.(1)												
#06	w/ \mathbf{Z}^B	8.30M	1.20G	.841	.753	.049	.821	.737	.067	.804	.654	.038
(e) Group Number $M \rightarrow$ see Equ.(2)												
#07	$M = 1$	8.30M	1.20G	.841	.756	.049	.822	.751	.064	.806	.662	.037
#08	$M = 4$	8.30M	1.20G	.842	.759	.048	.822	.742	.067	.809	.669	.036
#09	$M = 16$	8.30M	1.20G	.842	.752	.049	.829	.744	.065	.803	.651	.039
#10	$M = 32$	8.30M	1.20G	.845	.913	.047	.827	.745	.063	.809	.666	.036
(f) Scaling Factors $N \in \{N_1, N_2, N_3\} \rightarrow$ see Equ.(5)												
#11	$\{2, 4, 8\}$	8.31M	1.20G	.842	.755	.048	.821	.741	.065	.808	.663	.036
#12	$\{4, 8, 16\}$	8.30M	1.20G	.844	.762	.047	.823	.744	.065	.806	.666	.037
(g) Gradient-Induced Transition \rightarrow see Equ.(6)												
#13	w/o \mathcal{T}_i	8.31M	1.20G	.839	.748	.050	.825	.741	.065	.802	.649	.039

Contribution of Network Decoupling Strategy. We explore the necessity of our decoupling strategy. Inspired by [16], we replace the feature extracted from the texture encoder with the low-level feature \mathbf{X}_2 from the context encoder, which yields a single-stream network (#05). Notably, we only change the extracting manner of texture features and preserve the gradient-wise supervision for both variants (*i.e.*, #05 & #S) to ensure unbiased ablation. Table 5-(c) demonstrates that decoupling the network into two streams can improve the performance (F_β^w : +5.3% on CAMO-Test), which benefits from the modelling of separated branches without feature ambiguity at different hierarchies.

Contribution of Object Gradient Supervision. We replace the gradient map \mathbf{Z}^G (#S) with the boundary mask \mathbf{Z}^B (#06) for the supervision of the context learning process. The improvement (F_β^w : +1.7% on CAMO-Test) of our gradient map supervision further demonstrates the effectiveness. The first row of Fig. 8 presents the low-level features extracted from the texture learning branch under different supervision types. It shows that our solution can enforce the network to capture

**Fig. 8** Feature visualizations of two core designs, including the supervision of object gradient (1st row) and the GIT (2nd row).**Table 6** Training DGNet-S under the supervision of texture label (TINet-Text [34]) and our object gradient label (DGNet-Grad).

	NC4K-Test			CAMO-Test			COD10K-Test		
	S_α	F_β^w	\mathcal{M}	S_α	F_β^w	\mathcal{M}	S_α	F_β^w	\mathcal{M}
w/ TINet-Text	.839	.747	.050	.820	.731	.068	.803	.652	.040
w/ DGNet-Grad	.845	.764	.047	.826	.754	.063	.810	.672	.036

the gradient-sensitive information inside the camouflaged object’s body, where those pixels learn to draw the observer’s attention.

We further conduct the experiment using the supervision of texture label [34] (see Fig. 2), the

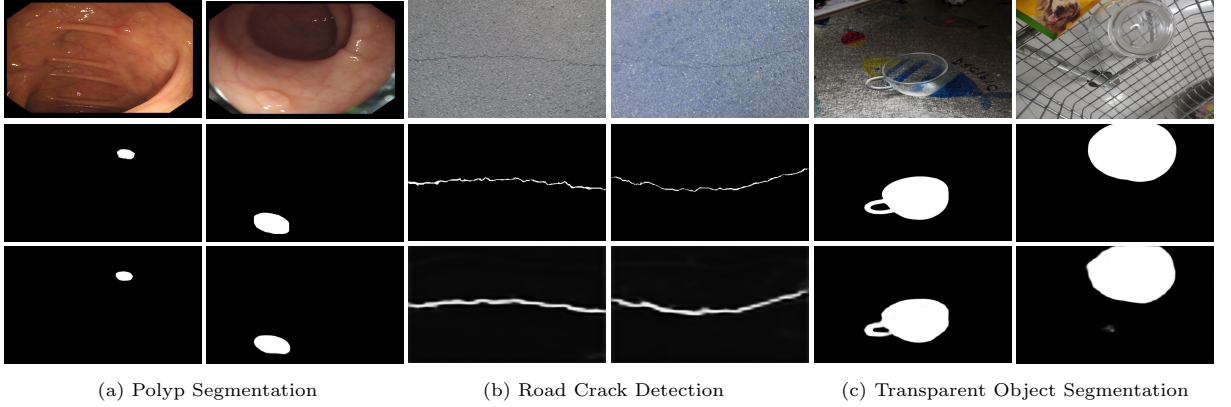


Fig. 9 Visualization results of three downstream applications. From top to bottom: input image (1st row), ground-truth (2nd row), and prediction (3rd row).

results in Table 6 demonstrate that our gradient-supervision manner (*i.e.*, w/ DGNet-Grad) is better than the texture-supervision (*i.e.*, w/ TINet-Text). Besides, our method is simpler and more efficient than TINet, *e.g.*, DGNet-S (8.0M) *vs.* TINet (28.6M), DGNet-S (80 fps) *vs.* TINet (50 fps). With such a compact design, we also achieve the new SOTA performance on CAMO-Test, *e.g.*, DGNet-S ($\mathcal{S}_\alpha = 0.826$), DGNet ($\mathcal{S}_\alpha = 0.839$) *vs.* TINet ($\mathcal{S}_\alpha = 0.781$).

Configuration of Group Numbers. In Table 5-(e), we report different variants with respect to four group numbers M , which are equal to 1 (#07), 4 (#08), 8 (#S), 16 (#09), and 32 (#10), respectively. Note that #07 ($M = 1$) means ungrouped candidate features, which causes degraded performance (F_β^w : -1.0% on COD10K-Test). We empirically choose $M = 8$ with the best performance.

Configuration of Scaling Factors. We also discuss how scaling factors $N \in \{N_1, N_2, N_3\}$ affect the model performance in Table 5-(f). Compared with different configurations (#11: {2, 4, 8} and #12: {4, 8, 16}), our finer-grained factors (#S: {8, 16, 32}) lead to better prediction performance. As shown in Fig. 4, we present the feature visualization of three parallel features (*i.e.*, $\mathbf{A}_i^{N_1}$, $\mathbf{A}_i^{N_2}$, and $\mathbf{A}_i^{N_3}$), where the network puts different attention weights on different parts of object insides. This also validates that parallel residual learning can further enhance the context feature from different group-aware perspectives.

Contribution of Gradient-Induced Transition. We replace the whole GIT with the naive channel-wise concatenation (#13: *w/o* \mathcal{T}_i) in our

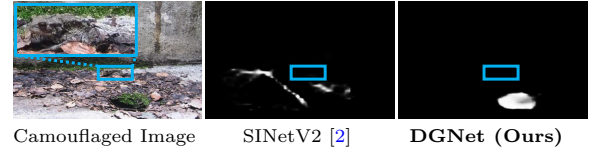


Fig. 10 Hard sample with small camouflaged object.

model to verify its effectiveness, which shows that our DGNet-S equipped with GIT (#S: *w/* \mathcal{T}_i) can improve 2.3% F_β^w on the COD10K-Test dataset. Moreover, as shown in the second-row of Fig. 8, the model obtains a cleaner and finer representation \mathbf{Z}_i^T (*i.e.*, (d) after GIT) while suppressing the noises in the background of \mathbf{X}_i^R (*i.e.*, (c) before GIT). A clear benefit of the adaptive aggregation of the context and texture cues in the GIT.

4.4 Limitation

Despite our method obtaining satisfactory performance, it may fail in challenging camouflaged scenarios with small objects. We argue that in the proposed strategy it is still difficult to provide enough texture cues in the limited target region, resulting in false-positive predictions. As shown in Fig. 10, such cases also easily confuses the rank@1 approach SINetV2 [2], thus deserving further studies.

5 Downstream Applications

In this section, we also assess the generalization capabilities on three downstream applications.

Polyp Segmentation. In the early diagnosis of colonoscopy, the low boundary contrast between

Table 7 Quantitative results on two popular polyp segmentation test datasets.

Baseline	CVC-ColonDB [68]				ETIS-LPDB [69]			
	S_α	$\uparrow E_\phi^{mx}$	$\uparrow F_\beta^w$	$\uparrow D^{mx}$	S_α	$\uparrow E_\phi^{mx}$	$\uparrow F_\beta^w$	$\uparrow D^{mx}$
UNet [70]	.710	.781	.491	.560	.684	.740	.366	.444
UNet++ [71]	.692	.764	.467	.550	.683	.776	.390	.509
PraNet [3]	.820	.872	.699	.728	.794	.841	.600	.639
MSNet [72]	.838	.883	.736	.766	.845	.890	.677	.736
[†] DGNet	.858	.898	.765	.789	.847	.904	.690	.741

a polyp and its highly-similar surroundings significantly decreases the detectability of colorectal cancer. To demonstrate the generality of our method in the medical field, we follow the same benchmark protocols as [3] and retrain our DGNet on the training set of Kvasir-SEG [73] and CVC-ClinicDB [74] datasets. We use two unseen test datasets: CVC-ColonDB [68] and ETIS-LPDB [69]. Table 7 shows that our [†]DGNet² consistently surpasses four cutting-edge polyp segmentation methods in four metrics, including S_α , E_ϕ^{mx} , F_β^w , and maximum Dice score (D^{mx}). Fig. 9 (a) shows the visualization results generated by our [†]DGNet.

Defect Detection. Substandard products (*e.g.*, tiles, wood) will inevitably incur unrecoverable economic losses in manufacturing. We further retrain our [†]DGNet on the road crack detection dataset (*i.e.*, CrackForest [75]), using 60% of the samples for training and 40% for testing. Fig. 9 (b) presents some visualization cases.

Transparent Object Segmentation. In daily life, intelligent agents such as robots and drones need to identify unnoticeable transparent objects (*e.g.*, glasses, bottles, and mirrors) to avoid accidents. We also verify the effectiveness of the retrained model [†]DGNet on the transparent object segmentation task. For convenience, we re-organize the annotation of the Trans10K [76] dataset from instance-level to object-level for training. The visual results shown in Fig. 9 (c) further demonstrate the learning ability of [†]DGNet.

6 Conclusion

We presented a novel deep gradient learning framework (**DGNet**) for efficiently segmenting camouflaged objects. To extract the camouflaged features, we proposed to decouple the task into two branches, a context encoder and a texture

encoder. We designed a novel plug-and-play module called gradient-induced transition (GIT), acting as a soft grouping module to jointly learn features from these two branches. This simple and flexible architecture showed strong generalization capabilities on three challenging datasets compared to the 20 SOTA competitors. In addition, our efficient version **DGNet-S** (8.3M & 80 fps) achieved an excellent performance-efficiency trade-off. Our solution also produced visually appealing results on three further applications, including polyp segmentation, defect detection, and transparent object segmentation, which validates its practical application value.

Acknowledgments

The authors would like to thank the anonymous reviewers and editor for their helpful comments on this manuscript.

Conflicts of Interests

The authors declared that they have no conflicts of interest in this work. We declare that we do not have any commercial or associative interest that represents a conflict of interest in connection with the work submitted.

References

- [1] D.-P. Fan, G.-P. Ji, G. Sun, M.-M. Cheng, J. Shen, and L. Shao, “Camouflaged object detection,” in *CVPR*, 2020.
- [2] D.-P. Fan, G.-P. Ji, M.-M. Cheng, and L. Shao, “Concealed object detection,” *IEEE TPAMI*, 2022.
- [3] D.-P. Fan, G.-P. Ji, T. Zhou, G. Chen, H. Fu, J. Shen, and L. Shao, “Pranet: Parallel reverse attention network for polyp segmentation,” in *MICCAI*, 2020.
- [4] G.-P. Ji, Y.-C. Chou, D.-P. Fan, G. Chen, D. Jha, H. Fu, and L. Shao, “Progressively normalized self-attention network for video polyp segmentation,” in *MICCAI*, 2021.
- [5] G.-P. Ji, G. Xiao, Y.-C. Chou, D.-P. Fan, K. Zhao, G. Chen, H. Fu, and L. Van Gool,

^{2†}DGNet denotes that we retrain DGNet on task-specific training dataset.

- “Deep learning for video polyp segmentation: A comprehensive study,” *arXiv*, 2022.
- [6] D.-P. Fan, T. Zhou, G.-P. Ji, Y. Zhou, G. Chen, H. Fu, J. Shen, and L. Shao, “Inf-net: Automatic covid-19 lung infection segmentation from ct images,” *IEEE TMI*, 2020.
- [7] Y.-H. Wu, S.-H. Gao, J. Mei, J. Xu, D.-P. Fan, R.-G. Zhang, and M.-M. Cheng, “Jcs: An explainable covid-19 diagnosis system by joint classification and segmentation,” *IEEE TIP*, 2021.
- [8] J. Liu, B. Dong, S. Wang, H. Cui, D.-P. Fan, J. Ma, and G. Chen, “Covid-19 lung infection segmentation with a novel two-stage cross-domain transfer learning framework,” *MIA*, 2021.
- [9] R. Feng and B. Prabhakaran, “Facilitating fashion camouflage art,” in *MM*, 2013.
- [10] M. Dean, R. Harwood, and C. Kasari, “The art of camouflage: Gender differences in the social behaviors of girls and boys with autism spectrum disorder,” *Autism*, 2017.
- [11] H. Mei, G.-P. Ji, Z. Wei, X. Yang, X. Wei, and D.-P. Fan, “Camouflaged object segmentation with distraction mining,” in *CVPR*, 2021.
- [12] Y. Lyu, J. Zhang, Y. Dai, A. Li, B. Liu, N. Barnes, and D.-P. Fan, “Simultaneously localize, segment and rank the camouflaged objects,” in *CVPR*, 2021.
- [13] Q. Jia, S. Yao, Y. Liu, X. Fan, R. Liu, and Z. Luo, “Segment, magnify and reiterate: Detecting camouflaged objects the hard way,” in *CVPR*, 2022.
- [14] Y. Zhong, B. Li, L. Tang, S. Kuang, S. Wu, and S. Ding, “Detecting camouflaged object in frequency domain,” in *CVPR*, 2022.
- [15] Q. Zhai, X. Li, F. Yang, C. Chen, H. Cheng, and D.-P. Fan, “Mutual graph learning for camouflaged object detection,” in *CVPR*, 2021.
- [16] G.-P. Ji, L. Zhu, M. Zhuge, and K. Fu, “Fast camouflaged object detection via edge-based reversible re-calibration network,” *PR*, 2022.
- [17] H. Zhu, P. Li, H. Xie, X. Yan, D. Liang, D. Chen, M. Wei, and J. Qin, “I can find you! boundary-guided separated attention network for camouflaged object detection,” in *AAAI*, 2022.
- [18] F. Yang, Q. Zhai, X. Li, R. Huang, A. Luo, H. Cheng, and D.-P. Fan, “Uncertainty-guided transformer reasoning for camouflaged object detection,” in *ICCV*, 2021.
- [19] A. Li, J. Zhang, Y. Lv, B. Liu, T. Zhang, and Y. Dai, “Uncertainty-aware joint salient object and camouflaged object detection,” in *CVPR*, 2021.
- [20] Y. Pan, Y. Chen, Q. Fu, P. Zhang, and X. Xu, “Study on the camouflaged target detection method based on 3d convexity,” *MAS*, 2011.
- [21] P. Sengottuvelan, A. Wahi, and A. Shanmugam, “Performance of decamouflaging through exploratory image analysis,” in *ICETET*, 2008.
- [22] Z. Liu, K. Huang, and T. Tan, “Foreground object detection using top-down information based on em framework,” *IEEE TIP*, 2012.
- [23] J. Y. Y. H. W. Hou and J. Li, “Detection of the mobile object with camouflage color under dynamic background based on optical flow,” *PE*, 2011.
- [24] J. Gallego and P. Bertolino, “Foreground object segmentation for moving camera sequences based on foreground-background probabilistic models and prior probability maps,” in *ICIP*, 2014.
- [25] Y. Sun, G. Chen, T. Zhou, Y. Zhang, and N. Liu, “Context-aware Cross-level Fusion Network for Camouflaged Object Detection,” in *IJCAI*, 2021.
- [26] G. Chen, S. Liu, Y. Sun, G.-P. Ji, Y. Wu, and T. Zhou, “Camouflaged object detection via context-aware cross-level fusion,” *IEEE*

TCSVT, 2022.

- [27] J. Ren, X. Hu, L. Zhu, X. Xu, Y. Xu, W. Wang, Z. Deng, and P.-A. Heng, “Deep texture-aware features for camouflaged object detection,” *arXiv preprint arXiv:2102.02996*, 2021.
- [28] N. Kajiura, H. Liu, and S. Satoh, “Improving camouflaged object detection with the uncertainty of pseudo-edge labels,” in *MM Asia*, 2021.
- [29] M. Zhuge, X. Lu, Y. Guo, Z. Cai, and S. Chen, “Cubenet: X-shape connection for camouflaged object detection,” *PR*, 2022.
- [30] T.-N. Le, T. V. Nguyen, Z. Nie, M.-T. Tran, and A. Sugimoto, “Anabranh network for camouflaged object segmentation,” *CVIU*, 2019.
- [31] Y. Pang, X. Zhao, T.-Z. Xiang, L. Zhang, and H. Lu, “Zoom in and out: A mixed-scale triplet network for camouflaged object detection,” in *CVPR*, 2022.
- [32] Y. Mao, J. Zhang, Z. Wan, Y. Dai, A. Li, Y. Lv, X. Tian, D.-P. Fan, and N. Barnes, “Transformer transforms salient object detection and camouflaged object detection,” *arXiv preprint arXiv:2104.10127*, 2021.
- [33] X. Cheng, H. Xiong, D.-P. Fan, Y. Zhong, M. Harandi, T. Drummond, and Z. Ge, “Implicit motion handling for video camouflaged object detection,” in *CVPR*, 2022.
- [34] J. Zhu, X. Zhang, S. Zhang, and J. Liu, “Inferring camouflaged objects by texture-aware interactive guidance network,” in *AAAI*, 2021.
- [35] T. Lin, P. Dollar, R. Girshick, K. He, B. Hariharan, and S. Belongie, “Feature pyramid networks for object detection,” in *CVPR*, 2017.
- [36] Z. Ke, J. Sun, K. Li, Q. Yan, and R. W. Lau, “Modnet: Real-time trimap-free portrait matting via objective decomposition,” in *AAAI*, 2022.
- [37] M. Tan and Q. Le, “Efficientnet: Rethinking model scaling for convolutional neural networks,” in *ICLR*, 2019.
- [38] S. Ioffe and C. Szegedy, “Batch normalization: Accelerating deep network training by reducing internal covariate shift,” in *ICML*, 2015.
- [39] X. Glorot, A. Bordes, and Y. Bengio, “Deep sparse rectifier neural networks,” in *ICAIIS*, 2011.
- [40] Z. Su, W. Liu, Z. Yu, D. Hu, Q. Liao, Q. Tian, M. Pietikainen, and L. Liu, “Pixel difference networks for efficient edge detection,” in *ICCV*, 2021.
- [41] C. Ma, Y. Rao, Y. Cheng, C. Chen, J. Lu, and J. Zhou, “Structure-preserving super resolution with gradient guidance,” in *CVPR*, 2020.
- [42] J. Canny, “A computational approach to edge detection,” *IEEE TAPMI*, 1986.
- [43] L.-C. Chen, G. Papandreou, I. Kokkinos, K. Murphy, and A. L. Yuille, “Deepplab: Semantic image segmentation with deep convolutional nets, atrous convolution, and fully connected crfs,” *IEEE TPAMI*, 2017.
- [44] K. He, X. Zhang, S. Ren, and J. Sun, “Deep residual learning for image recognition,” in *CVPR*, 2016.
- [45] J. Wei, S. Wang, and Q. Huang, “F³net: Fusion, feedback and focus for salient object detection,” in *AAAI*, 2020.
- [46] A. Paszke, S. Gross, F. Massa, A. Lerer, J. Bradbury, G. Chanan, T. Killeen, Z. Lin, N. Gimelshein, L. Antiga *et al.*, “Pytorch: An imperative style, high-performance deep learning library,” in *NeurIPS*, 2019.
- [47] S.-M. Hu, D. Liang, G.-Y. Yang, G.-W. Yang, and W.-Y. Zhou, “Jittor: a novel deep learning framework with meta-operators and unified graph execution,” *Science China Information Sciences*, 2020.

- [48] K. He, X. Zhang, S. Ren, and J. Sun, “Delving deep into rectifiers: Surpassing human-level performance on imagenet classification,” in *ICCV*, 2015.
- [49] A. Krizhevsky, I. Sutskever, and G. E. Hinton, “Imagenet classification with deep convolutional neural networks,” in *NeurIPS*, 2012.
- [50] D. P. Kingma and J. Ba, “Adam: A method for stochastic optimization,” in *ICLR*, 2015.
- [51] I. Loshchilov and F. Hutter, “Sgdr: Stochastic gradient descent with warm restarts,” in *ICLR*, 2017.
- [52] P. Krähenbühl and V. Koltun, “Efficient inference in fully connected crfs with gaussian edge potentials,” in *NeurIPS*, 2011.
- [53] D.-P. Fan, M.-M. Cheng, Y. Liu, T. Li, and A. Borji, “Structure-measure: A New Way to Evaluate Foreground Maps,” in *ICCV*, 2017.
- [54] D.-P. Fan, C. Gong, Y. Cao, B. Ren, M.-M. Cheng, and A. Borji, “Enhanced-alignment measure for binary foreground map evaluation,” in *IJCAI*, 2018.
- [55] D.-P. Fan, G.-P. Ji, X. Qin, and M.-M. Cheng, “Cognitive vision inspired object segmentation metric and loss function,” *SSI*, 2021.
- [56] A. Borji, M.-M. Cheng, H. Jiang, and J. Li, “Salient object detection: A benchmark,” *IEEE TIP*, 2015.
- [57] M. Zhuge, D.-P. Fan, N. Liu, D. Zhang, D. Xu, and L. Shao, “Salient object detection via integrity learning,” *IEEE TPAMI*, 2022.
- [58] R. Margolin, L. Zelnik-Manor, and A. Tal, “How to evaluate foreground maps?” in *CVPR*, 2014.
- [59] A. Borji, M.-M. Cheng, H. Jiang, and J. Li, “Salient object detection: A benchmark,” *IEEE TIP*, 2015.
- [60] J.-X. Zhao, J.-J. Liu, D.-P. Fan, Y. Cao, J. Yang, and M.-M. Cheng, “Egnet: Edge guidance network for salient object detection,” in *ICCV*, 2019.
- [61] Z. Wu, L. Su, and Q. Huang, “Stacked cross refinement network for edge-aware salient object detection,” in *ICCV*, 2019.
- [62] Z. Wu, L. Su, and Q. Huang, “Cascaded partial decoder for fast and accurate salient object detection,” in *CVPR*, 2019.
- [63] S.-H. Gao, Y.-Q. Tan, M.-M. Cheng, C. Lu, Y. Chen, and S. Yan, “Highly efficient salient object detection with 100k parameters,” in *ECCV*, 2020.
- [64] J. Zhang, D.-P. Fan, Y. Dai, S. Anwar, F. Sadat Saleh, T. Zhang, and N. Barnes, “UC-Net: Uncertainty Inspired RGB-D Saliency Detection via Conditional Variational Autoencoders,” in *CVPR*, 2020.
- [65] H. Zhou, X. Xie, J.-H. Lai, Z. Chen, and L. Yang, “Interactive two-stream decoder for accurate and fast saliency detection,” in *CVPR*, 2020.
- [66] Y. Pang, X. Zhao, L. Zhang, and H. Lu, “Multi-scale interactive network for salient object detection,” in *CVPR*, 2020.
- [67] X. Qin, D.-P. Fan, C. Huang, C. Diagne, Z. Zhang, A. C. Sant’Anna, A. Suarez, M. Jagersand, and L. Shao, “Boundary-aware segmentation network for mobile and web applications,” *arXiv preprint arXiv:2101.04704*, 2021.
- [68] J. Bernal, J. Sánchez, and F. Vilarino, “Towards automatic polyp detection with a polyp appearance model,” *PR*, 2012.
- [69] J. Silva, A. Histace, O. Romain, X. Dray, and B. Granado, “Toward embedded detection of polyps in wce images for early diagnosis of colorectal cancer,” *IJCARS*, 2014.
- [70] O. Ronneberger, P. Fischer, and T. Brox, “U-net: Convolutional networks for biomedical image segmentation,” in *MICCAI*, 2015.

- [71] Z. Zhou, M. M. R. Siddiquee, N. Tajbakhsh, and J. Liang, “UNet++: A nested U-Net architecture for medical image segmentation,” *IEEE TMI*, 2019.
- [72] X. Zhao, L. Zhang, and H. Lu, “Automatic polyp segmentation via multi-scale subtraction network,” in *MICCAI*, 2021.
- [73] D. Jha, P. H. Smedsrud, M. A. Riegler, P. Halvorsen, T. de Lange, D. Johansen, and H. D. Johansen, “Kvasir-seg: A segmented polyp dataset,” in *ICMM*, 2020.
- [74] J. Bernal, F. J. Sánchez, G. Fernández-Esparrach, D. Gil, C. Rodríguez, and F. Vilariño, “Wm-dova maps for accurate polyp highlighting in colonoscopy: Validation vs. saliency maps from physicians,” *CMIG*, 2015.
- [75] Y. Shi, L. Cui, Z. Qi, F. Meng, and Z. Chen, “Automatic road crack detection using random structured forests,” *IEEE TITS*, 2016.
- [76] E. Xie, W. Wang, W. Wang, M. Ding, C. Shen, and P. Luo, “Segmenting transparent objects in the wild,” in *ECCV*, 2020.